SANDIA REPORT
SAND2013-9770
Unlimited Release
November 2013

A Comparison of the Lattice Discrete Particle Method to the Finite-Element Method and the K&C Material Model for Simulating the Static and Dynamic Response of Concrete

Jovanca J. Smith, Joseph E. Bishop

Prepared by
Sandia National Laboratories
Albuquerque, New Mexico 87185 and Livermore, California 94550

Sandia National Laboratories is a multi-program laboratory managed and operated by Sandia Corporation, a wholly owned subsidiary of Lockheed Martin Corporation, for the U.S. Department of Energy's National Nuclear Security Administration under contract DE-AC04-94AL85000.

Sandia National Laboratories

Issued by Sandia National Laboratories, operated for the United States Department of Energy by Sandia Corporation.

Printed in the United States of America. This report has been reproduced directly from the best available copy.

Available to DOE and DOE contractors from
U.S. Department of Energy
Office of Scientific and Technical Information
P.O. Box 62
Oak Ridge, TN 37831

Telephone: (865) 576-8401
Facsimile: (865) 576-5728
E-Mail: reports@adonis.osti.gov
Online ordering: http://www.osti.gov/bridge

Available to the public from
U.S. Department of Commerce
National Technical Information Service
5285 Port Royal Rd.
Springfield, VA 22161

Telephone: (800) 553-6847
Facsimile: (703) 605-6900
E-Mail: orders@ntis.fedworld.gov
Online order: http://www.ntis.gov/help/ordermethods.asp?loc=7-4-0#online

SAND2013-9770
Unlimited Release
November 2013

A Comparison of the Lattice Discrete Particle Model to the K&C Concrete Model with Applications to Dynamic Simulations

Jovanca J. Smith, Joseph E. Bishop
Computational Structural Mechanics
Sandia National Laboratories
P.O. Box 5800
Albuquerque, New Mexico 87185

Abstract

This report summarizes the work performed by the graduate student Jovanca Smith during a summer internship in the summer of 2012 with the aid of mentor Joe Bishop. The projects were a two-part endeavor that focused on the use of the numerical model called the Lattice Discrete Particle Model (LDPM). The LDPM is a discrete meso-scale model currently used at Northwestern University and the ERDC to model the heterogeneous quasi-brittle material, concrete.

In the first part of the project, LDPM was compared to the Karagozian and Case Concrete Model (K&C) used in Presto, an explicit dynamics finite-element code, developed at Sandia National Laboratories. In order to make this comparison, a series of quasi-static numerical experiments were performed, namely unconfined uniaxial compression tests on four varied cube specimen sizes, three-point bending notched experiments on three proportional specimen sizes, and six triaxial compression tests on a cylindrical specimen.

The second part of this project focused on the application of LDPM to simulate projectile perforation on an ultra high performance concrete called CORTUF. This application illustrates the strengths of LDPM over traditional continuum models.

CONTENTS

LIST OF FIGURES

LIST OF TABLES

1. INTRODUCTION

The complex nature of concrete is a result of the material's heterogeneous make-up, and quasi-brittle features. Therefore, to successfully model this composite, a numerical model that captures these qualities is necessary in order to accurately predict the response of the material to applied forces as well as obtain an accurate failure pattern.

In addition to the softening response of the cementitious composites, another major feature that is necessary for the accurate representation is the failure response. There are numerous models that can capture the stress strain response of the material like cohesive crack models, smeared crack models, and other non-local continuum models, but discrete models naturally capture the failure patterns because of their ability to represent the concrete aggregate and interphase layers.

The discrete numerical model adopted in this study is the Lattice Discrete Particle Model formulated, calibrated and validated by Cusatis and coworkers. The model operates at the meso-scale (10^{-2} – 10^{-3} m), and it explicitly represents the coarse aggregate particles as rigid spheres, within polyhedral cells. Each polyhedral cell contains an aggregate particle with surrounding matrix. Rigid body kinematics defines the material behavior, and it is the ability of LDPM to represent each individual coarse aggregate particle that produces realistic failure patterns.

A continuum model naturally uses fewer degrees of freedom than its discrete counterpart and is computationally less expensive. This oftentimes makes the model more attractive to analysts. However, without the ability to model each specific component of the concrete mixture (example aggregate particles and fibers), as in a discrete model, certain important phenomena are neglected.

This first part of this report compares the continuum based Karagozian and Case (K&C) material model to the discrete numerical Lattice Discrete Particle Model (LDPM). Special emphasis is placed on the peak and post peak response of both models and comparison is made with experimental results. The ability to represent the accurate failure pattern and capture the peak load, softening and hardening response of concrete under specific loading conditions is investigated. Tests performed in this comparison are unconfined uniaxial compression test, 3-point bending tests, and triaxial compression tests. The ability of the K&C model to converge under mesh refinement is also investigated in this study.

The intrinsic capability of LDPM to explicitly represent the microstructural features of CORTUF, e.g. the steel fibers, is of interest to several groups at Sandia. For a demonstration, we simulated the perforation of CORTUF by a 50-caliber APM2 bullet.

2. REVIEW OF NUMERICAL MODELS

In this chapter both the LDPM and the K&C models are described in detail.

2.1. The Lattice Discrete Particle Model

The Lattice Discrete Particle Model (LDPM) is a meso-scale numerical model for concrete that can accurately represent concrete fracture in the elastic, hardening, and softening regimes. The LDPM is a synthesis of the Confinement Shear Lattice (CSL) Model by Cusatis (Cusatis et al. 2003, 2006, 2007) and the Discrete Particle Model (DPM) by Pelessone (Pelessone 2005). The connection of aggregate particles through a lattice system, granulometric distribution of aggregate particles, three-dimensional polyhedral cell, meso-scale constitutive behavior and the mechanical interaction of particles are all features inherited from the CSL model. However, the DPM contributed the explicit computational framework MARS (Modeling and Analysis of the Response of Structures) (Cusatis 2011).

In comparison to continuum material models, like the K&C model, LDPM can explicitly model fracture and fragmentation processes. LDPM can replicate the randomness of the crack surface, as well as splitting cracks observed in compression driven tensile failure (for example with uniaxial unconfined compression tests). This behavior is demonstrated in chapter 3.

In LDPM, the distribution of the numerical aggregate particles is performed via a granulometric distribution of the aggregates. The coarse aggregates are assumed to be idealized spheres allowing their representation with a particle size distribution function, a cumulative distribution function and a Fuller curve. For a given aggregate to cement ratio, water content, specimen volume, and maximum and minimum aggregate size, the total number of particles in the volume can be determined (Cusatis 2011).

The geometric idealization of the concrete mesostructure is displayed in Figure 1. The coarse aggregates are shown as the particle spheres, while the mortar, shown as the area between the particles in Figure 1, includes the fine aggregates. A Delaunay tetrahedralization connects the center of the particles (nodes), after which a dual domain tessellation is applied to form a polyhedral cell (see Figure 2). The polyhedral cell is the geometric representation of the aggregate and surrounding mortar. The triangular faces on the exterior of the cells are termed facets. Discrete compatibility and constitutive equations are applied on the facets, and it is the point of interaction of adjacent polyhedral cells.

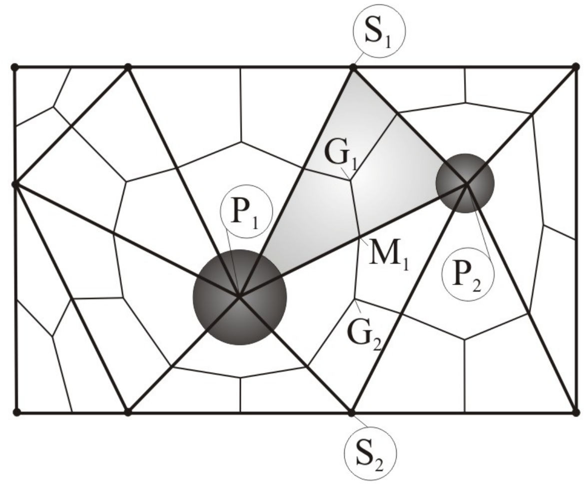

Figure 1. Geometrical representation of concrete mesostructure.

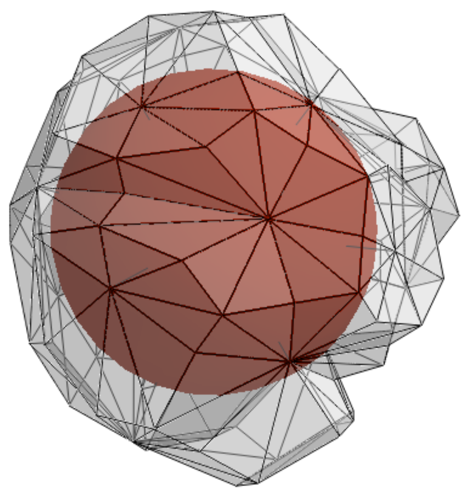

Figure 2. Polyhedral cell representing a coarse aggregate and surrounding mortar

For a force applied to the polyhedral cells that preserves elastic behavior, the strains, ε_n, and stresses, σ_N, are as defined as

$$\boldsymbol{\varepsilon_n} = \frac{\boldsymbol{n^T}[\![\boldsymbol{u}]\!]}{\boldsymbol{L}} \quad \boldsymbol{\varepsilon_m} = \frac{\boldsymbol{m^T}[\![\boldsymbol{u}]\!]}{\boldsymbol{L}} \quad \boldsymbol{\varepsilon_l} = \frac{\boldsymbol{l^T}[\![\boldsymbol{u}]\!]}{\boldsymbol{L}} \tag{1}$$

$$\boldsymbol{\sigma_N} = \boldsymbol{E_N \varepsilon_N} \quad \boldsymbol{\sigma_M} = \boldsymbol{E_T \varepsilon_M} \quad \boldsymbol{\sigma_L} = \boldsymbol{E_T \varepsilon_L} \tag{2}$$

where *n* represent the vector component normal to the facet, *m* and *l* represent the shear component on the facets, $[\![u]\!]$ is the displacement jump separation between facets associated with two neighboring aggregate particles, E_N is the Young's modulus, and E_T is the shear modulus, which is equal to a constant alpha, α, multiplied by E_N.

For strains beyond the elastic limit, the meso-scale crack opening, *w*, is given by

$$w = w_N n + w_M m + w_L l \tag{3}$$

where $w_N = l(\varepsilon_N - \sigma_N/E_N)$; $w_M = l(\varepsilon_M - \sigma_M/E_T)$; $w_L = l(\varepsilon_L - \sigma_L/E_T)$.

The tensile fracturing behavior in LDPM is formulated through the effective stress, σ, and effective strain, ε, given by

$$\sigma^2 = \sigma_N^2 + \frac{(\sigma_M + \sigma_L)^2}{\alpha} \quad ; \qquad \sigma = \sqrt{\sigma_N^2 + \frac{(\sigma_M + \sigma_L)^2}{\alpha}} \tag{4}$$

$$\varepsilon^2 = \varepsilon_N^2 + (\varepsilon_M^2 + \varepsilon_L^2)\alpha \ ; \qquad \varepsilon = \sqrt{\varepsilon_N^2 + (\varepsilon_M^2 + \varepsilon_L^2)\alpha} \ . \tag{5}$$

Using the effective stresses and strains, the normal and shear stresses conjugate to the normal and shear strains are given by

$$\sigma_N = \frac{\sigma}{\varepsilon}\varepsilon_N \tag{6}$$

$$\sigma_M = \frac{\sigma}{\varepsilon}\varepsilon_N\alpha \quad ; \quad \sigma_L = \frac{\sigma}{\varepsilon}\varepsilon_L\alpha. \tag{7}$$

The effective stress is incrementally elastic. This means $\dot{\sigma} = E_0\dot{\varepsilon}$, and σ must satisfy $0 \le \sigma \le \sigma_{bt}(\varepsilon, \omega)$. The strain dependent stress boundary, σ_{bt} is given by

$$\sigma_{bt}(\varepsilon, \omega) = \sigma_0(\omega) exp\left[-H_0(\omega)\frac{\langle \varepsilon_{max} - \varepsilon_0(\omega)\rangle}{\sigma_0(\omega)}\right] \tag{8}$$

where $\langle x \rangle = \max(x, 0)$, and ω is as defined by the equation,

$$\tan(\omega) = \frac{\varepsilon_N}{\sqrt{\alpha}\varepsilon_T} = \frac{\sigma_N\sqrt{\alpha}}{\sigma_T}. \tag{9}$$

The stress boundary, σ_{bt}, is an exponential function of the maximum effective strain. The softening modulus function, $H_0(\omega)$, has built into it a dependence on the length of the lattice element to preserve the correct energy dissipation during softening behavior. The tensile length l_t and shear length l_s are related to the meso-scale tensile fracture energy, G_t, and the meso-scale shear fracture energy, G_s, by the following equations respectively,

$$l_t = \frac{2E_0G_t}{\sigma_t^2} \tag{10}$$

$$l_s = \frac{2\alpha E_0 G_s}{\sigma_s^2}. \tag{11}$$

Additionally, the maximum effective strain is a history dependent variable, and it is defined as

$$\varepsilon_{max} = \sqrt{\varepsilon_{N,max}^2 + \alpha\varepsilon_{T,max}^2} \tag{12}$$

where $\varepsilon_{N,max}(t) = max[\varepsilon_N(\tau)] \quad for\ \tau < t$ and $\varepsilon_{T,max}(t) = max[\varepsilon_T(\tau)]$.

For compressive loading, the normal strain is less than 0, $\varepsilon_N < 0$, and the strain dependent stress boundary, $\sigma_{bc}(\varepsilon_D, \varepsilon_V) \leq \sigma_N \leq 0$ is a function of the deviatoric and the volumetric strains. The ratio of the deviatoric strains to the volumetric strains is given by r_{DV}, where ($r_{DV} = \varepsilon_D/\varepsilon_V$).

For a constant r_{DV}, $\sigma_{bc}(r_{DV}, \varepsilon_V)$ is assumed to be initially linear and hence models pore collapse. Compaction and re-hardening are modeled by an exponential evolution,

$$\sigma_{bc} = \begin{cases} \sigma_{c0} + \langle -\varepsilon_V - \varepsilon_{c0} \rangle H_c & \varepsilon_V \leq -\varepsilon_{c1} \\ \sigma_{c1}\, exp[(-\varepsilon_V - \varepsilon_{c1})H_c/\sigma_{c1}] & \varepsilon_V > -\varepsilon_{c1} \end{cases} \tag{13}$$

where σ_{c0} is the yielding compressive stress, ε_{c0} is the volumetric strain at the onset of pore collapse, H_c is the initial hardening modulus, ε_{c1} is the volumetric strain at which re-hardening begins, λ_{c0} is the material parameter that governs the onset of re-hardening, and $\sigma_{c1} = \sigma_{c0} + (\varepsilon_{c1} - \varepsilon_{c0})H_c$.

For an increase in the r_{DV}, slope of H_{c0} goes to 0 to get the plateau observed experimentally. The initial hardening modulus is defined as

$$H_c(r_{DV}) = \frac{H_{c0}}{1 + K_{c2}\langle r_{DV} - K_{c1} \rangle} \tag{14}$$

where $H_{c0} = K_{co}E_N$ and K_{co}, K_{c1}, K_{c2} are material properties.

In the presence of compressive stresses, frictional effects result in an increase in the shear strength. Incremental plasticity is used in LDPM to simulate these effects. The relationship between the incremental shear stresses and the incremental plastic shear strains are given by

$$\dot{\sigma_M} = E_T(\dot{\varepsilon_M} - \dot{\varepsilon_M^P}) \tag{15}$$

$$\dot{\sigma_L} = E_T(\dot{\varepsilon_L} - \dot{\varepsilon_L^P}). \tag{16}$$

The plastic strain increments are assumed to obey the normality rules

$$\dot{\varepsilon_M^P} = \dot{\lambda}\frac{\partial\varphi}{\partial\sigma_M} \tag{17}$$

$$\dot{\varepsilon}_L^P = \dot{\lambda}\frac{\partial\varphi}{\partial\sigma_L} \tag{18}$$

where λ is the plastic multiplier, and φ is the plastic potential given by $\sqrt{\sigma_M^2 + \sigma_L^2} - \sigma_{bs}(\sigma_N)$ with σ_{bs} being the shear strength obtained from a non-linear frictional law given in equation 19. The equations governing the shear strength are completed by the following loading-unloading conditions: $\varphi\dot{\lambda} \leq 0$ and $\dot{\lambda} \geq 0$.

$$\sigma_{bs} = \sigma_s + (\mu_0 - \mu_\infty)\sigma_{N0} - \mu_\infty\sigma_N - (\mu_0 - \mu_\infty)\sigma_{N0}\exp\left({}^{\sigma_N}/_{\sigma_{N0}}\right) \tag{19}$$

where σ_s is the cohesion, μ_0 is the initial friction coefficient, μ_∞ is the final friction coefficient, and σ_{N0} is the normal stress which the friction coefficients transition from the initial to the final friction.

There is strain rate dependence in the LDPM model that allows it to handle highly dynamic loading. The effect is accounted for by scaling the tensile stress-strain boundary and the cohesion by a function of the strain rate as given in equations 20 and 21.

$$\sigma_t^{dyn} = F(\dot{\varepsilon})\sigma_0(\omega)exp\left[-H_0(\omega)\frac{\langle\varepsilon_{max} - \varepsilon_0\omega\rangle}{\sigma_0(\omega)}\right] \tag{20}$$

$$\sigma_s^{dyn} = \sigma_s F(\dot{\varepsilon}) \tag{21}$$

where $F(\dot{\varepsilon}) = \left[1 + c_1 a\sinh\frac{\dot{\varepsilon}}{c_0}\right]$, and the parameters c_0 and c_1 are material properties.

The LDPM model currently does not contain an equation of state, and does not model shock phenomenon. Since concrete fragmentation occurs under high dynamic loading, which is quite different from steel, and LDPM focuses on concrete fracture, the equation of state can be neglected.

Further details on the LDPM model can be found in the references Cusatis et al. 2003, 2006, 2007, and 2011.

2.2. The K&C Model

The K&C model is a stress-strain material model used in finite element simulations. The K&C model assumes that concrete is homogeneous and initially isotropic. It decouples the volumetric and deviatoric response of the material. When a material is in the elastic regime, all the distortion energy is recovered upon unloading. For loading that takes the material into the plastic regime, only elastic distortion energy is recovered upon unloading as the material permanently deforms. The function used for the material's transition from elastic to plastic, is termed the yield criterion, and is given by

$$\sqrt{J_2} = F_f(I_1, \theta, \kappa), \tag{22}$$

where $\sqrt{J_2}, I_1$ and θ are stress invariants, and κ represents the internal state variables.

The peak stress limit of the K&C model is described by the limit surface and the residual surface. The limit surface provides a boundary in the model for stresses that are achievable at least one time. After this stress state is achieved, the extent of damage results in a new achievable stress state that is less than the limit surface and continues to decrease until it gets to a residual stress surface. Hence, the yield surface provides the threshold for the elastic stresses, after which the material hardens or softens to reach the limit and residual surfaces respectively. In the K&C model, these surfaces are uncapped along the pressure axis. It is important to note that the internal state variables of the specimen allow for the change of the yield surface while the limit and residual surfaces remain constant. Figure 3 shows the yield surface of the K&C model without a cap. The absence of a cap in the model means that no limit exists for the yield surface at high pressure and the effect of porosity on shear strength is excluded in the model. Due to this effect, all three surfaces in the K&C model are fixed and their equations are given by

$$\text{Yield surface} \qquad \Delta\sigma_y = a_{0y} + \frac{p}{a_{1y} + a_{2y}p} \tag{23}$$

$$\text{Limit surface} \qquad \Delta\sigma_m = a_{0m} + \frac{p}{a_{1m} + a_{2m}p} \tag{24}$$

$$\text{Residual surface} \qquad \Delta\sigma_r = a_{0f} + \frac{p}{a_{1f} + a_{2f}p} \tag{25}$$

where *a* parameters are user inputs and *p* are pressures.

After the initial yield surface is attained, an interpolation between equations 23 and 24 provides the current surface,

$$\Delta\sigma = \eta\left(\Delta\sigma_m - \Delta\sigma_y\right) + \Delta\sigma_y \tag{26}$$

$$F(I_1) = \eta\left(\mathrm{F}_m(I_1) - \mathrm{F}_y(I_1)\right) + \mathrm{F}_y(I_1) \tag{27}$$

where η is a user defined damage function, and a function of the plastic strain parameter with relationship as shown in Figure 4.

The strain rate enhancement factor of the model, which is a dynamic increasing factor (DIF), is used to scale the strength surfaces in the model for rate effects. Rate effects are used in the K&C model to capture shear damage accumulation.

The K&C model has been updated numerous times by various agencies, and much detail on the model can be found in the literature (Brannon 2009), (Malvar 1996).

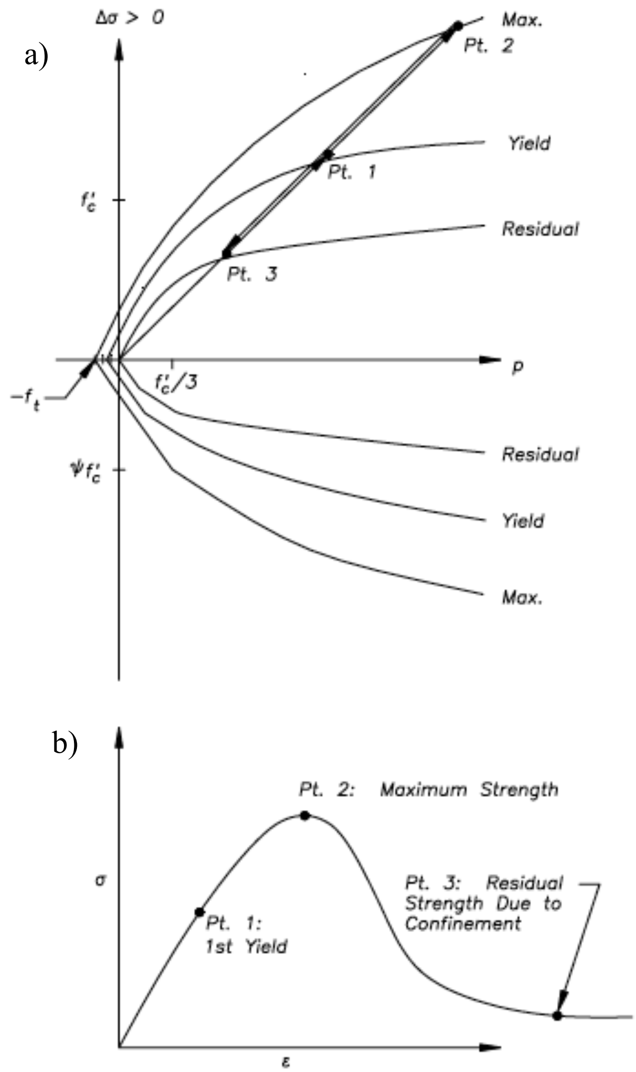

Figure 3. Yield surface for the K&C model (Malvar 1996) showing (a) stress-pressure, and (b) stress-strain plots

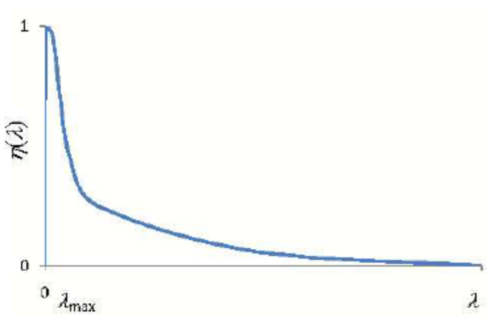

Figure 4. Function of the user defined damage function, η on the y-axis as a function of the plastic strain parameter on the x-axis (Brannon 2009)

3. K&C AND LDPM MODEL COMPARISON

For convenience, material tests were chosen that were already performed and used to calibrate and validate the LDPM model (Cusatis 2011). The implementation of the K&C model in Presto is fully parameterized by the unconfined compressive strength. For the K&C model, the compressive strength for the concrete materials chosen were 38 MPa, 35 MPa, and 68 MPa for the uniaxial compression tests, triaxial tests, and 3 point bending tests respectively as determined experimentally. The static parameters used for the LDPM concrete model are given in (Cusatis 2011). The following sub-sections describe the various tests are describe the uniaxial compression test, triaxial compression test, and 3 point bending test.

3.1. The Uniaxial Compression Test

In the uniaxial compression test (UC) an axial force is applied to the specimen without any radial constraint as shown in Figure 5 (Vasconelos 2008). The test can be done in both load and displacement control, but to obtain the post-peak softening response, the displacement-controlled test must be used. Four block specimens of various sizes were used. Each specimen had a cross section of 100 mm x 100 mm with varying heights as shown in Figure 6.

Figure 5. Test setup for unconfined uniaxial compression test (Vasconelos 2008)

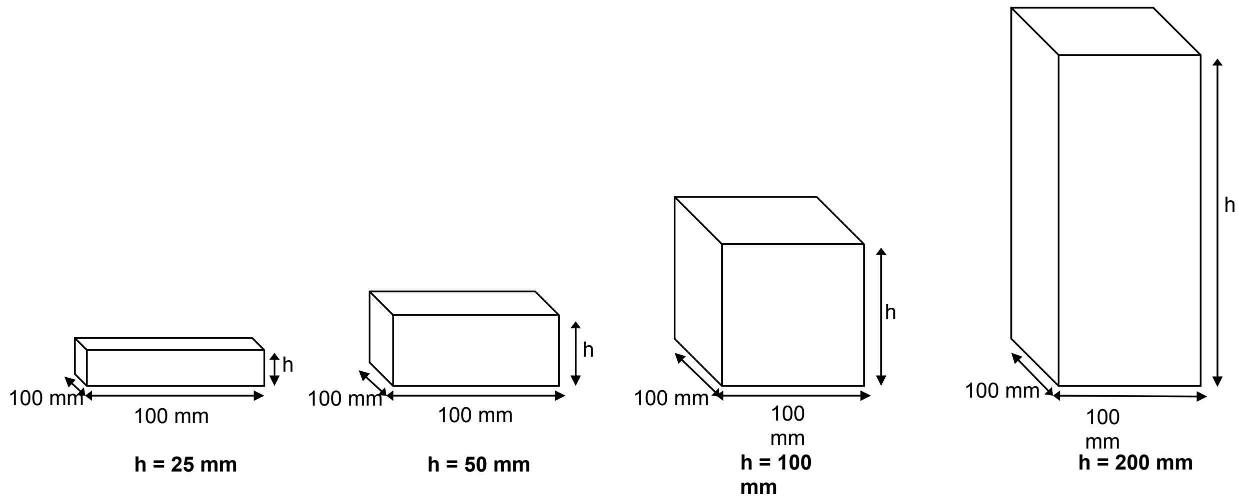

Figure 6. Specimen sizes used in unconfined uniaxial compression tests by Vasconelos

3.1.1. Simulation Setup for the Lattice Discrete Particle Model

To simulate the experimental set up using the LDPM model, the velocity of the steel plate in contact with the specimen was prescribed. A low friction contact response was implemented in the contact algorithm between the plate and the specimen. For each simulation, the axial force and displacement were obtained and used to determine the axial stress and strain response. The results are shown later and described in detail in section 3.1.3.

3.1.2. Simulation of the Finite Element Method and the K&C Material Model

For the finite-element method using the K&C material model, velocity boundary conditions were applied to the nodes on the top surface of the specimen, and thus no contact or friction algorithm was needed. This approximation is justified since the tests were performed in a low friction setting.

Several meshes (see Table 1) were used to investigate any mesh dependence in the solution. Figures of the various mesh sizes are shown in Figure 7 through Figure 10. The mesh density in each coordinate direction was chosen to maintain a finite-element aspect ratio of one.

Table 1. Mesh densities for UC block specimens

Mesh name	Specimen height (25 mm)	Specimen height (50 mm)	Specimen height (100 mm)	Specimen height (200 mm)
mesh 1			**1 x 1 x 1**	**1 x 1 x 2**
mesh 2		**2 x 2 x 1**	**2 x 2 x 2**	**2 x 2 x 4**
mesh 4	**4 x 4 x 1**	**4 x 4 x 2**	**4 x 4 x 4**	**4 x 4 x 8**
mesh 8	**8 x 8 x 2**	**8 x 8 x 4**	**8 x 8 x 8**	**8 x 8 x 16**
mesh 16	**16 x 16 x 4**	**16 x 16 x 8**	**16 x 16 x 16**	**16 x 16 x 32**
mesh 32	**32 x 32 x 8**	**32 x 32 x 16**	**32 x 32 x 32**	**32 x 32 x 64**
mesh 64	**64 x 64 x 16**	**64 x 64 x 32**	**64 x 64 x 64**	**64 x 64 x 128**

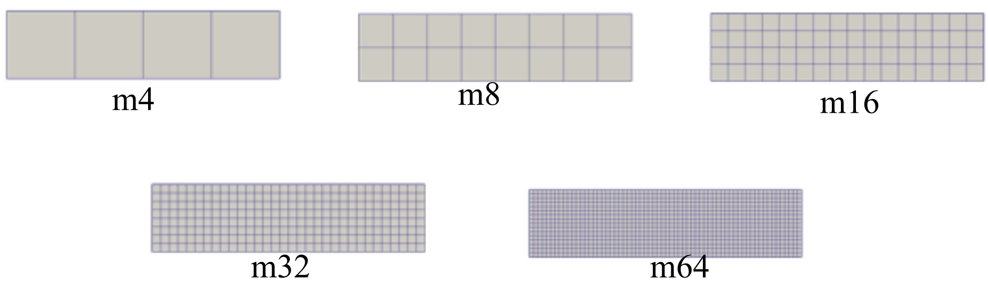

Figure 7. Finite element meshes used in the simulation of the UC test with specimen height of 25 mm

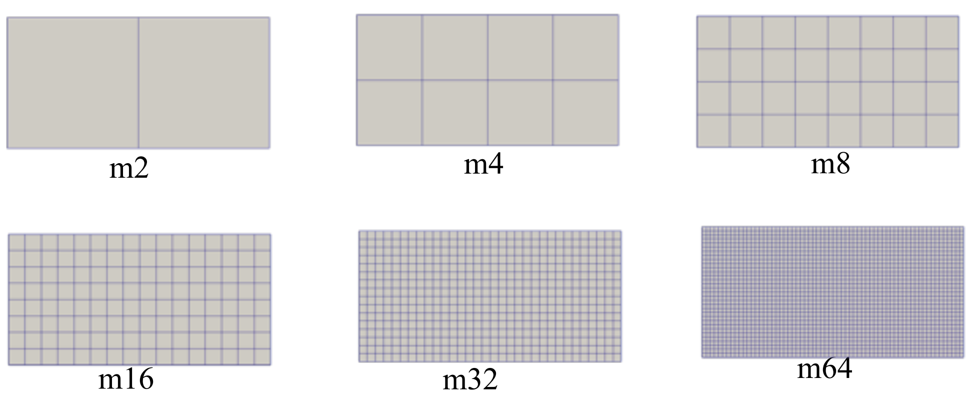

Figure 8. Finite element meshes used in the simulation of the UC test with specimen height of 50 mm

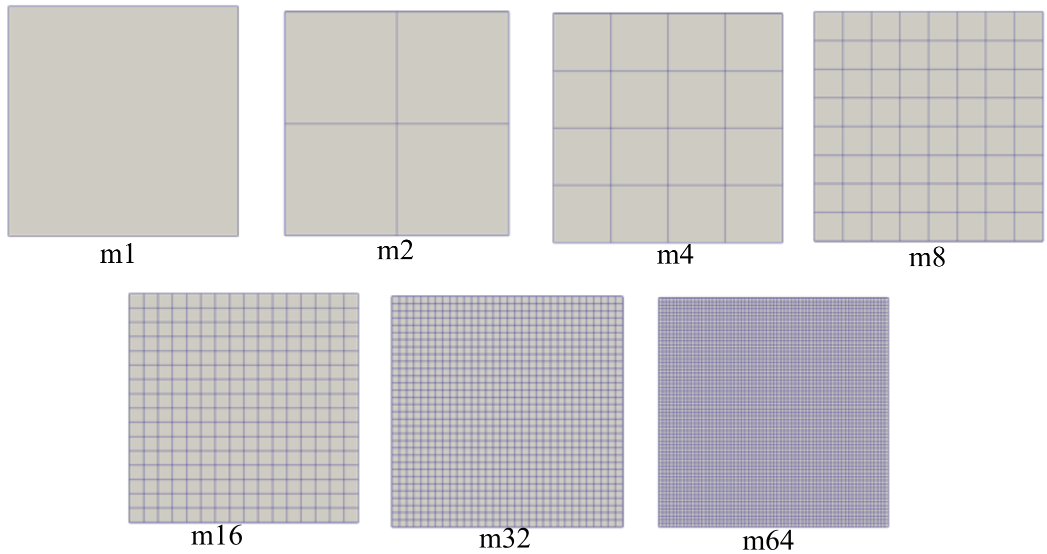

Figure 9. Finite element meshes used in the simulation of the UC test with specimen height of 100 mm

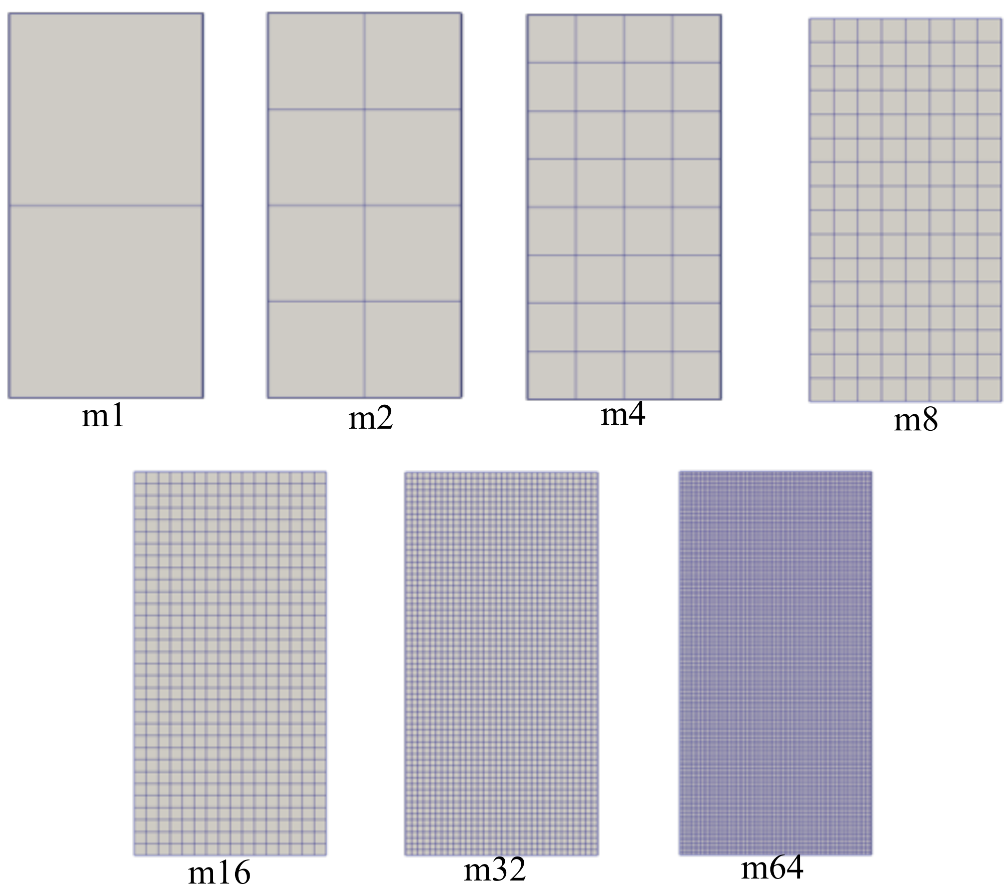

Figure 10. Finite element meshes used in the simulation of the UC test with specimen height of 200 mm

3.1.3. Uniaxial Compression Simulation Results and Discussion

Figure 11a-d shows the axial stress versus axial strain response for the uniaxial compression test for specimens with varying heights, 25 mm, 50 mm, 100 mm, and 200 mm respectively. As previously described in section 3.1.1, the axial force and displacement are recovered directly from the test. The stress is calculated by dividing the force by the cross sectional area of the specimen, while the strain is the extension divided by the original specimen length. The LDPM can accurately capture the response of the UC test in the elastic, peak, and softening regime. The K&C model accurately captured the modulus and the peak stress. However, the post peak response was not captured. For the smallest specimen height, the K&C model was able to converge with mesh refinement, but as the specimen height increased, the model became mesh dependent.

The failure pattern observed in Figure 12 for the LDPM model shows a splitting type failure that is expected in the UC test. Under axial compression, tensile forces develop in the radial direction causing failure parallel to the axis of loading. The LDPM model accurately captured this phenomenon. The K&C model was unable to display the crack pattern. Instead, the maximum principal stresses are captured and the result is shown in Figure 13.

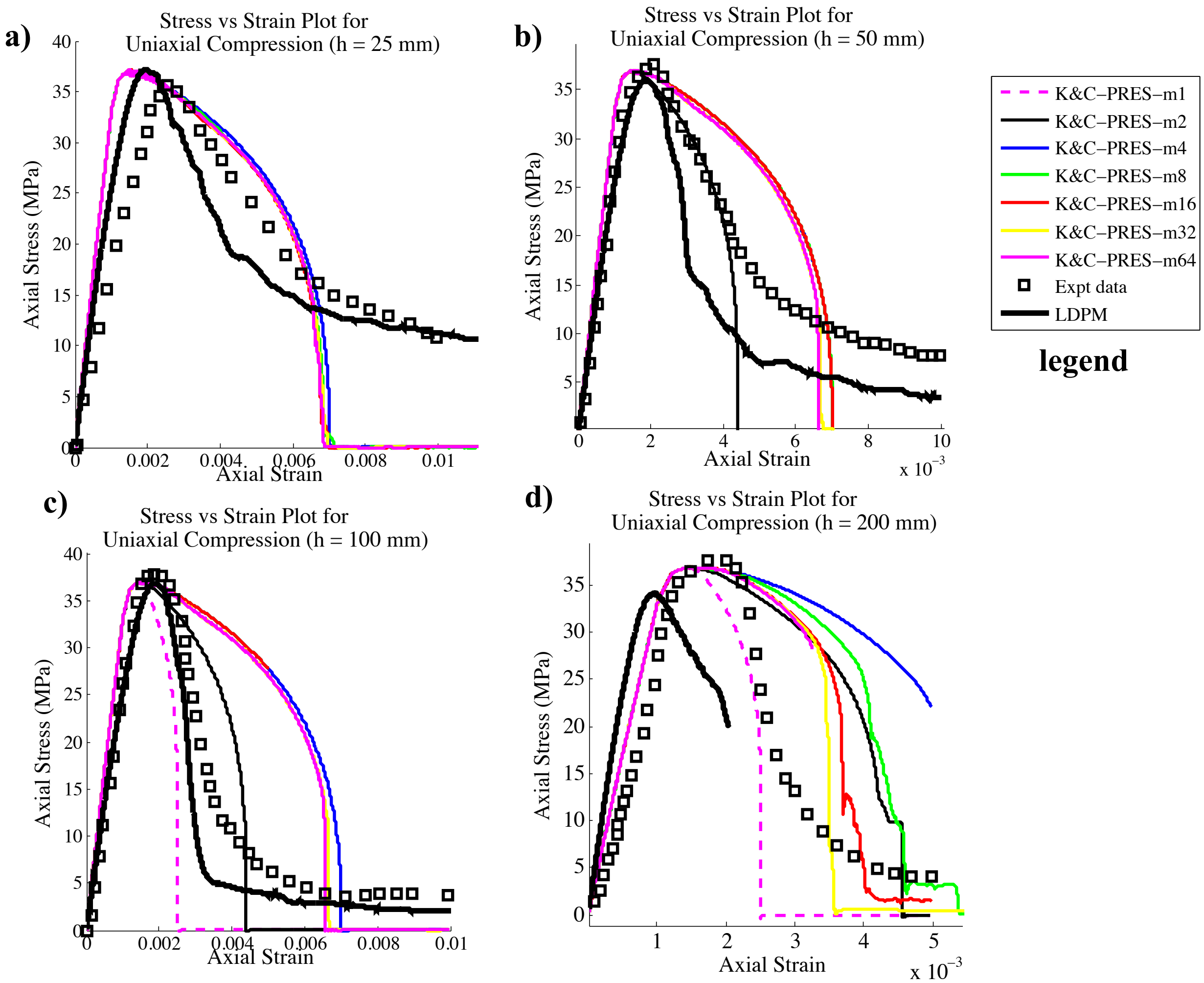

Figure 11. Stress-strain results comparing the LDPM and K&C model are given for several levels of mesh refinement

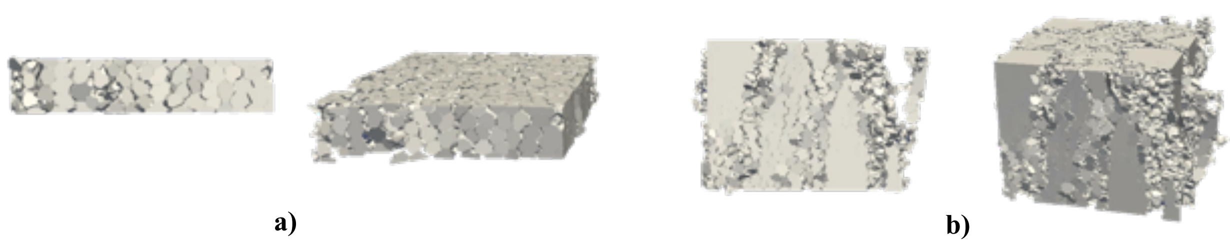

Figure 12. Failure crack pattern for UC test for LDPM with heights a) 25 mm and b) 100 mm

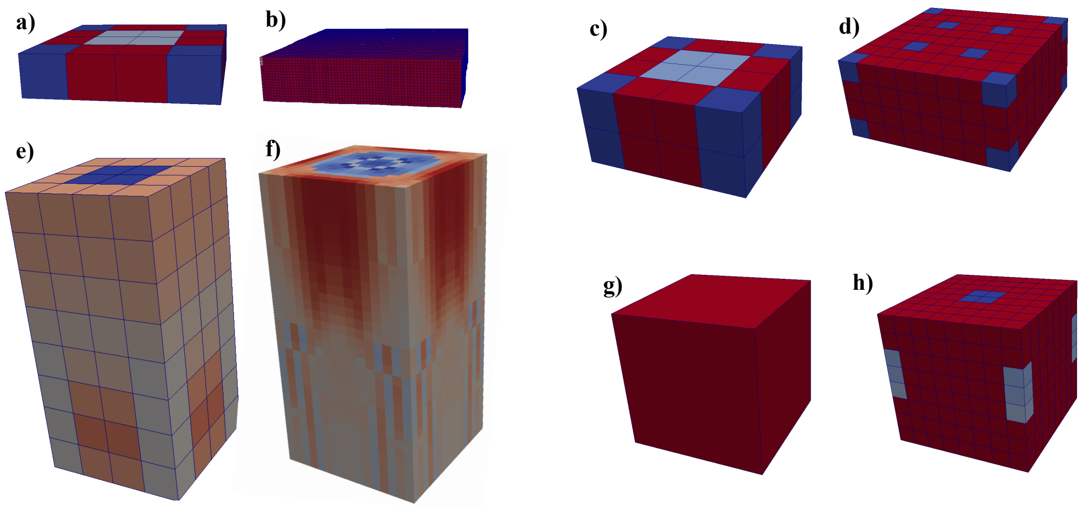

Figure 13. Stress variation in UC test specimen for K&C Model for varying specimen sizes and mesh sizes a-b) 25 mm, c-d) 50 mm, e-f) 200 mm, g-h) 100 mm

3.2. The Triaxial Compression Test

A cylindrical specimen with a diameter of 76.2 mm (3 in) and a height of 152.4 mm (6 in) was used in the triaxial compression (TXC) tests. The TXC is performed in 2 parts. In the first part, the hydrostatic phase, a confinement pressure is applied to the cylinder until a specified pressure, and in the second phase, while holding the hydrostatic pressure constant, an additional force was applied axially. Six varying confinements were used in the TXC tests: 60 MPa, 30MPa, 9 MPa, 4.5 MPa, 1.5 MPa, and 0 MPa. The 0 MPa TXC test is similar to the UC test. The experimental test setup for the TXC test is shown in Figure 14.

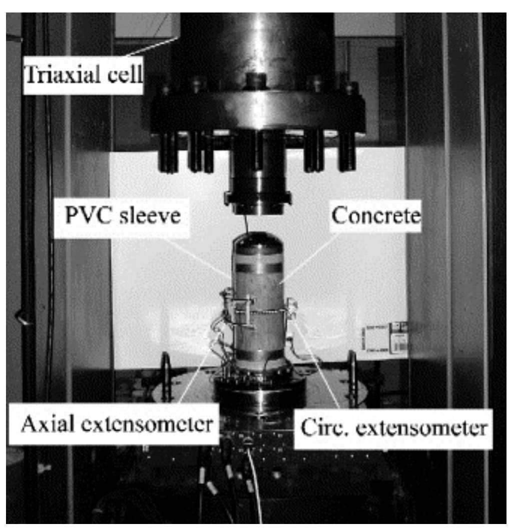

Figure 14. Experimental test setup for TXC test (Lu 2006)

3.2.1. Setup for the Lattice Discrete Particle Model

The LDPM simulation of the TXC test was performed in two stages identical to the experimental test setup. In the first stage, a uniform pressure was applied to the test cylinder and the equivalent velocity on the outer cylindrical surface was recorded. In the second phase, the outer velocities recorded in the first phase were reapplied to the outer cylindrical surface nodes on the cylindrical specimen until the specified pressure was obtained, and a velocity was applied axially to the specimen at the same rate as the cylindrical velocity. The test was performed under low friction as in the UC test. The LDPM TXC tests were not in this instance performed by the author, but the LDPM TXC stress strain response was taken from the plots in (Cusatis 2011).

3.2.2. Test Setup for the K&C Model

The K&C test setup was performed similar to the LDPM format. The test was carried out in two separate phases. In the first instance, a hydrostatic pressure was applied to the specimen, and the velocity on the top surface was recorded. For the second portion of the test, the pressure was reapplied at the same rate to the outer cylindrical specimen surface, while simultaneously applying an axial velocity to the top surface nodes. The pressure on the cylindrical surface was held constant when it reached the specified pressure, and the axial velocity was applied. Three meshes were used on for each of the TXC tests (see Figure 15) to test for mesh dependence.

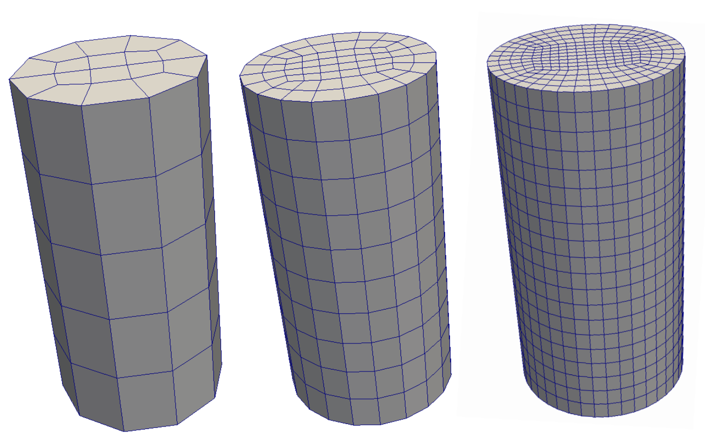

Figure 15. Mesh sizes for the K&C model for the TXC test

3.2.3. Triaxial Compression Test Results and Observations

The stress versus strain plots of the TXC tests are shown in Figure 16 using both LDPM and K&C models. The LDPM model captures the elastic response, peak and post peak for the TXC test. It does overestimate the response of the material in the lower pressure problems. The K&C model captured the elastic and peak response well for the triaxial tests with confining pressures up to 9 MPa, but after initial softening, the tail re-hardens. This behavior could be altered if the user had full exposure to the input parameters. Additionally, the K&C model overestimated the peak and post peak response of the higher-pressure tests in the TXC simulations.

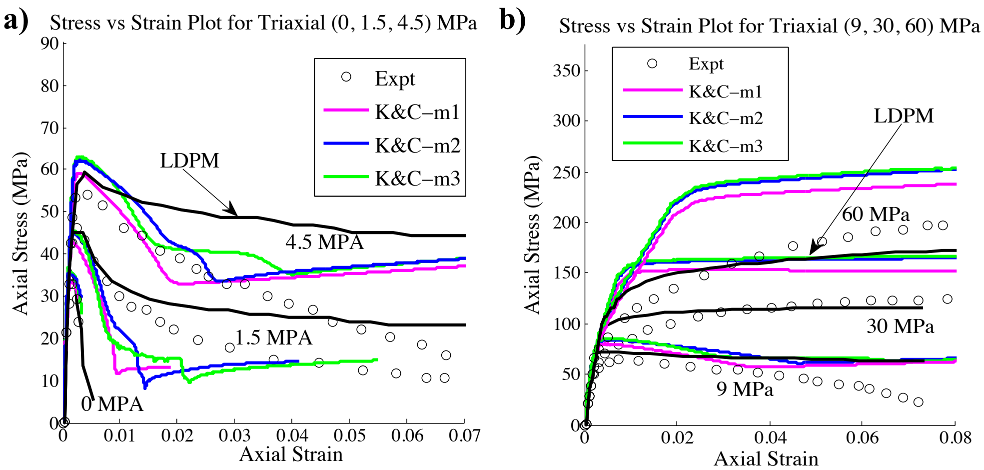

Figure 16. Stress strain response of the triaxial compression test for LDPM and K&C

3.3. The 3-Point Bending Test

The experimental setup for 3-point bending test (3pt) is shown in Figure 17. In the 3pt a load is applied to the top center of the specimen with a cylindrical steel rod, and the bottom left and right edges are placed onto an additional rod. This setup allows the center of the specimen to be displaced and less displacement towards the end until finally no displacement at the boundary conditions (supports) at the two bottom ends of the specimen. The test is usually performed in displacement control mode to capture the post peak response. The three point notched bending tests were performed using the three specimen sizes shown in Figure 18. The three specimen sizes all maintained the same width but the height, span, and notch height were all scaled to test the ability of the models to capture size effect.

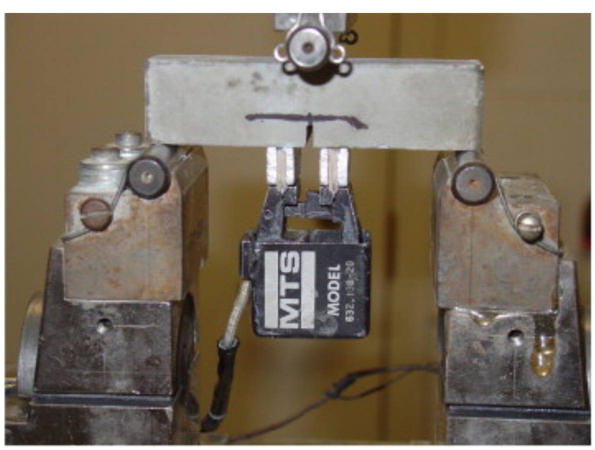

Figure 17. Experimental test setup for 3-point bending test (M. S. Konsta-Gdoutos 2010)

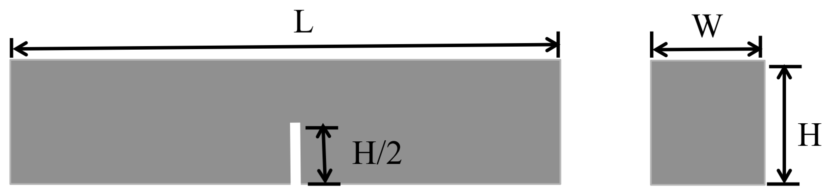

	L (mm)	W (mm)	H (mm)
Small	800	100	100
Medium	1131	100	200
Large	1386	100	300

Figure 18. Specimen size for 3-point bending tests

3.3.1. Test Setup for the Lattice Discrete Particle Model

For the LDPM simulation of the 3pt, a velocity was applied to the top centerline nodes, and the boundary conditions were applied to the support nodes to maintain zero vertical displacement at the ends of the specimen in the direction of loading. Since the model contained no fiber reinforcement that would cause the failure to be distributed, the expected failure was a localized crack originating at the notch tip. Hence, the portion of the specimen modeled with LDPM was reduced only to 100 mm in the center of the specimen and finite elements were used to model the surrounding matrix that was uncracked.

3.3.2. Test Setup for the K&C Model

For the finite element based K&C model, the test setup was similar to the setup used in the LDPM model. Instead of the velocity being applied to the top nodes, the velocity was uniformly applied to the top surface the width of the notch (4 mm). The supports were modeled by applying zero displacement to the edge nodes on the far left and right of the specimen.

3.3.2. Results and Observations for the 3-Point Bending Tests

The LDPM captured the response of the concrete material in tension quite accurately. The elastic, peak, and post peak results match the experimental data (see Figure 19). However, the K&C model underestimated the tensile response of the material by about two thirds of the experimental data. Additionally, in the K&C plots, there is a re-hardening phenomenon occurring due to the fact that the compressive stresses on the top of the specimen above the notch of the can no longer be distributed with the selected mesh size (see Figure 22 and Figure 23) due to the transition of stress from compressive to tensile. This can be reduced if the mesh is further refined.

The LDPM failure modes clearly demonstrate the crack pattern observed for concrete with no reinforcement. The crack is very localized and originates from the center of the specimen due to the presence of the notch (see Figure 20 and Figure 21).

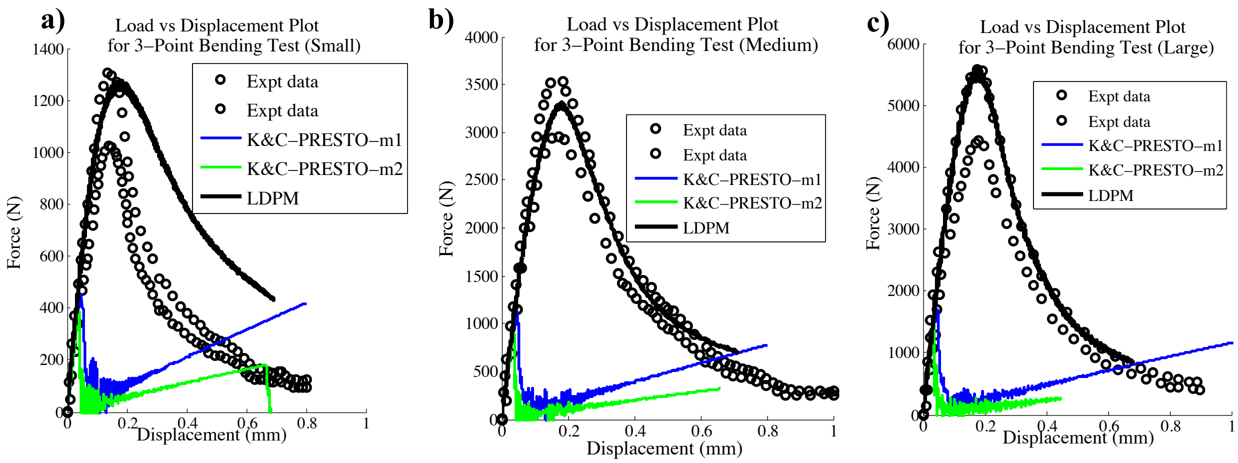

Figure 19. Load displacement curve for 3 point bending test a) Small b) Medium c) Large

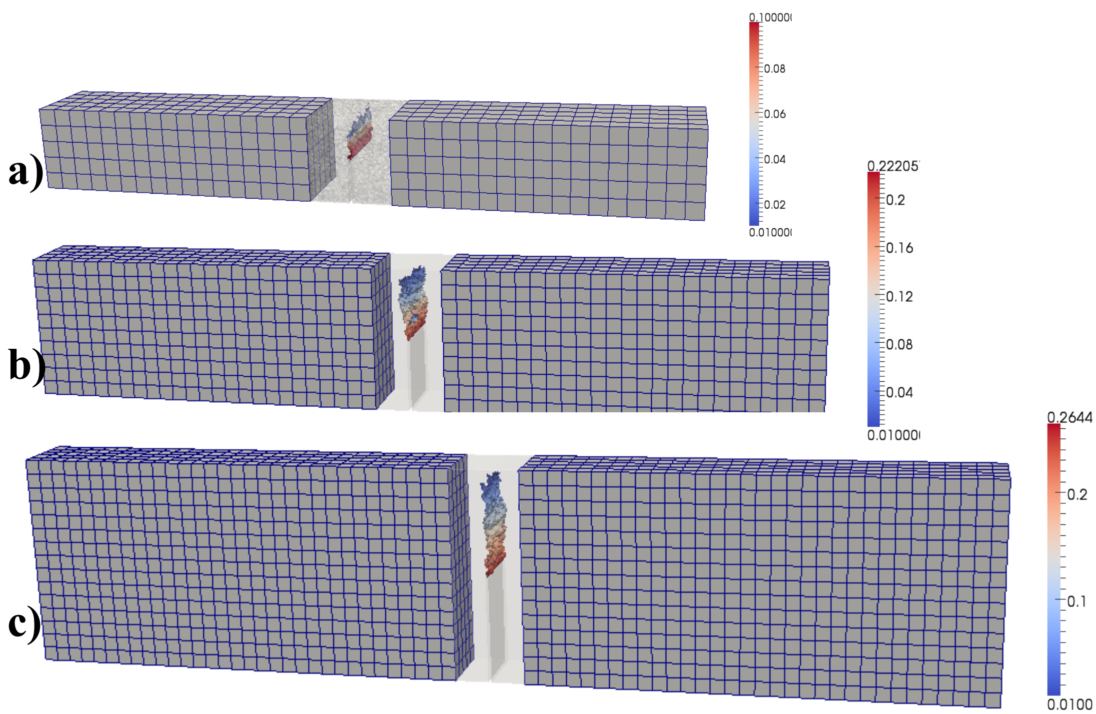

Figure 20. Failure mode showing crack opening for 3 point bending test using the LDPM model a) Small b) Medium c) Large specimens

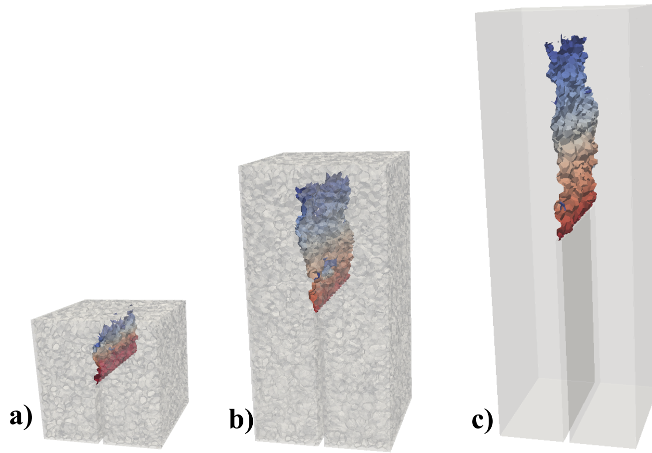

Figure 21. Failure mode showing crack for 3 point bending test with LDPM – LDPM center portion only a) Small b) Medium c) Large

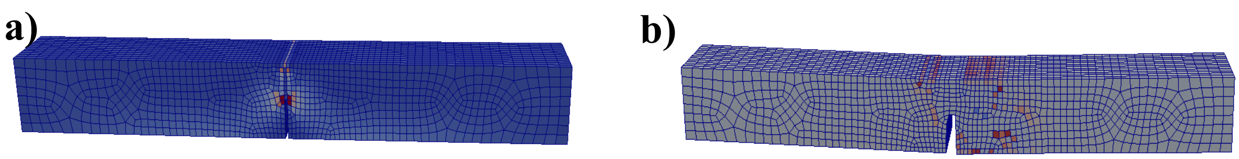

Figure 22. Stress and Damage for K&C model for 3pt size small a) max principal stress at softening for mesh1, b) max principal stress at re-hardening for mesh 1

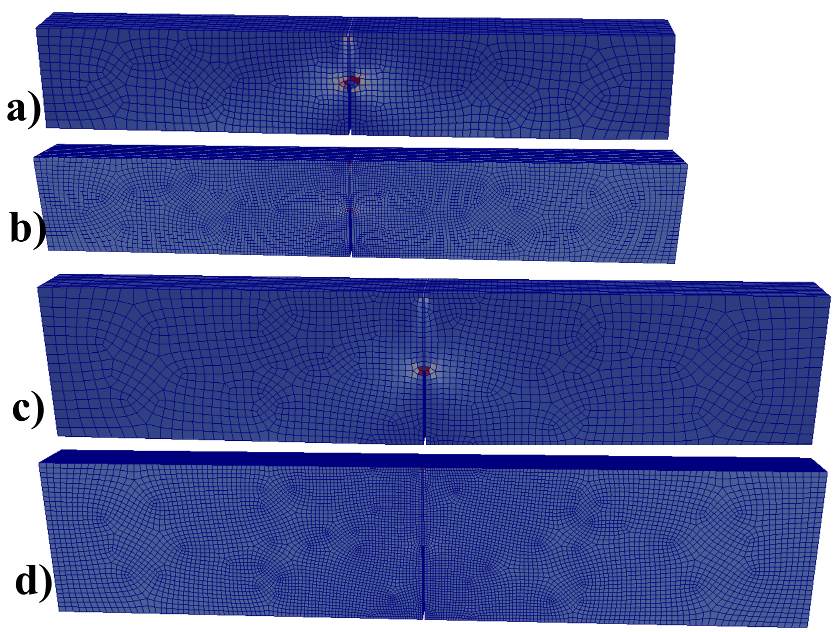

Figure 23. Maximum principal stress for K&C model for 3pt a) medium mesh 1, b) medium mesh 2, c) large mesh 1, d) large mesh 2

A final phenomenon investigated in the 3 point bending tests was size effect. Size effect is a decrease in the stress of the material when the specimen increases in size. In order to investigate this response in the models, the height of the specimen and the notch height had to be scaled to maintain proper proportion with the specimen height, since varying heights can produce diverse results. To make a comparison of strength, the normalized stress, σ_t and strain, ε_t response was obtained from the load, P and displacement, D for all three specimens using the following equations

$$\sigma_t = \frac{3PL}{2WH^2} \tag{28}$$

$$\varepsilon_t = \frac{6DH}{L^2}. \tag{29}$$

Figure 24a demonstrates that for an increase in specimen size, there is a decrease in strength in the LDPM model showing it can model the size effect. Additionally, Figure 24b, demonstrates that the K&C model also captured this effect although the strength was incorrect.

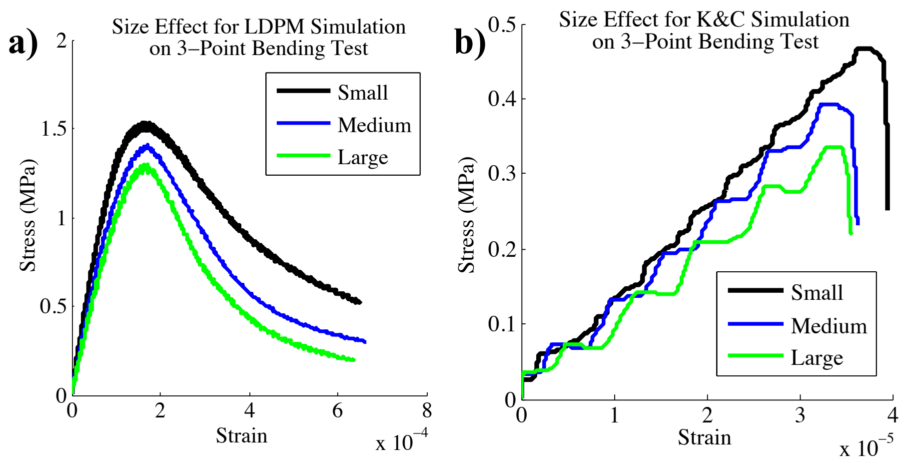

Figure 24. Size effect results for a) LDPM model b) K&C model

4. APPLICATION OF LDPM MODEL TO PERFORATION

Recently, new capabilities have been added to LDPM in order to accurately simulate ultra-high performance concrete (Smith 2012). The first author investigated the ability of LDPM to capture the response of projectile penetration and perforation experiments on a high performance concrete using a flat nose fragment-simulating penetrator. This section uses the LDPM model to characterize the behavior of CORTUF concrete under perforation.

4.1. CORTUF

Perforation (complete penetration of the projectile through the specimen) analysis was performed on ultra high performance concrete panels. CORTUF, the concrete specimen used is also termed a reactive powder concrete because the size of the aggregate particles is limited to silica sand (0.6 mm). The compressive strength of CORTUF ranges from about 170 MPa to 244 MPa. CORTUF comes either plain or reinforced with fibers. The fiber reinforcement used in CORTUF is ZP 305 hooked steel fibers with average length and diameter of 30 mm and 0.5 mm respectively. The volume fraction of the fiber-reinforced specimen is found to be about 3%. The material was previously calibrated and validated by the author on numerous quasi-static and dynamic experiments, and the parameters were used from the previous experiments to help with the time constraint (Smith 2012). It is important to note, that the actual size of CORTUF large aggregates were 0.6 mm, and these aggregates were coarse grained to 4 mm in this project. Coarse graining is a technique used to determine an equivalent parameter set for larger aggregate sizes. This technique considerable reduces the computation cost and time. However, the crack with for actual failure pattern in the experiments is smaller than the one obtained numerically.

4.2. LDPM Perforation Simulations

In these experiments, the target panel dimensions are 304.8 mm x 304.8 mm x 76.2 mm (12 in x 12 in x 3 in). The target was impacted by an ogive nose projectile. The projectile was a 50-caliber APM2 bullet and contained a steel core, a lead nose and a brass-gliding jacket. The total mass was 42 grams. For simplicity, only the inner core was modeled and the core dimensions are shown in Figure 25.

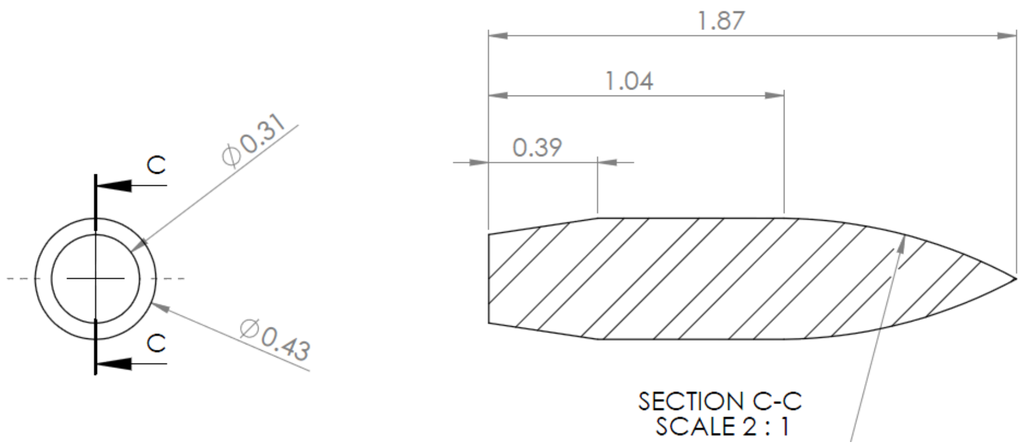

Figure 25. Schematic of the inner core APM2 projectile (all dimensions are in inches)

Simulation results for two different impact velocities were investigated: 960 m/s and 1500 m/s. Cubit was used to create a hex mesh as shown in Figure 26. The tip of the projectile experienced severe deformation, which caused numerical issues. Therefore, the projectile was modeled as a rigid bullet. This assumption was made because the core was made of high strength steel and very little deformation of the bullet was observed in the experiments. Additionally, modeling the projectile as a rigid material saved time in the simulations.

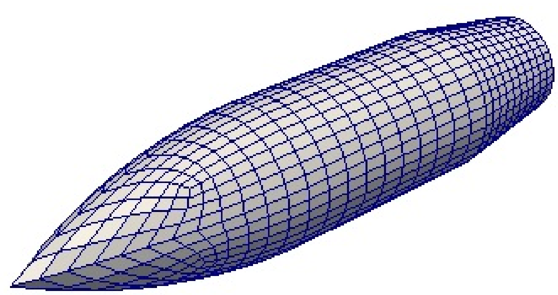

Figure 26. Hex mesh used for inner core of projectile

Various analyses were performed for the perforation simulations that included pitch and yaw rotations of the projectile is shown in Figure 27. The angle of obliquity (AoO), i.e. the angle the projectile at the point of contact makes with the orientation x-axis (see Figure 28), was also varied in the analysis. The fibers were oriented random, parallel, and perpendicular to the projectile axis (see Figure 29). The preferential direction is achieved with an ellipsoid function, allowing the probability of fibers in one direction, to be greater than the probability in another direction. The various perforation simulations performed are summarized in Table 2.

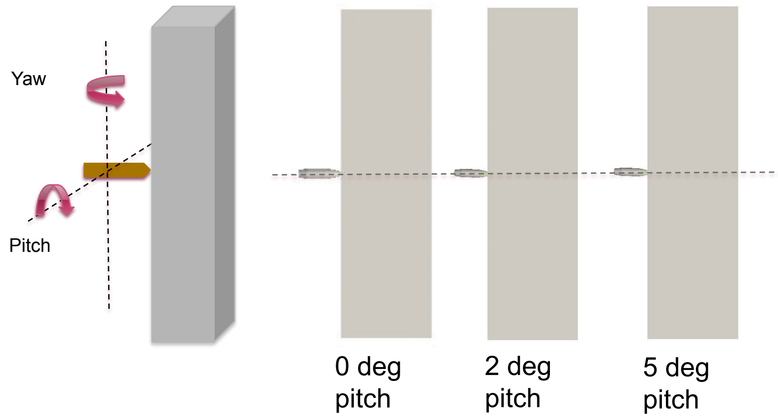

Figure 27. Pitch and Yaw Rotation of Projectile

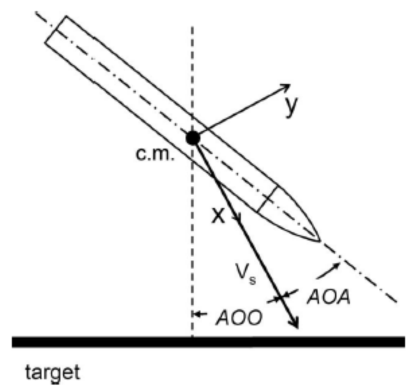

Figure 28. Figure showing the angle of obliquity (AoO) of an arbitrary projectile (J. E. Bishop 2009)

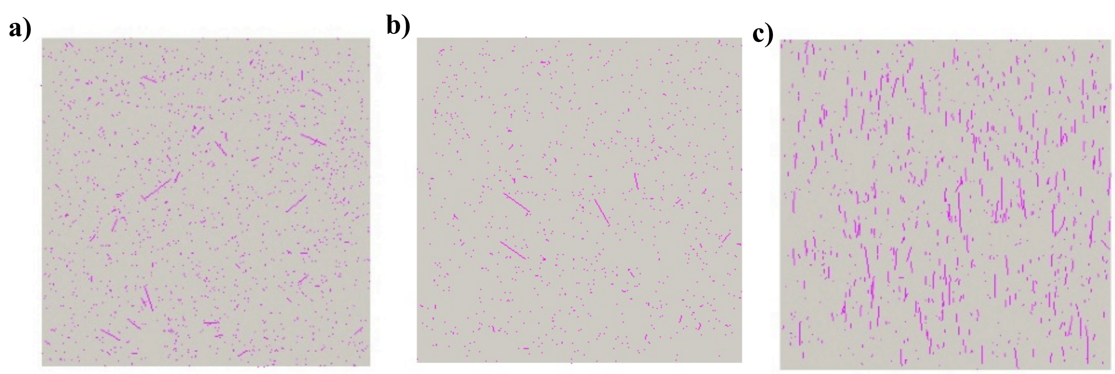

Figure 29. Front view of panel showing preferential fiber orientation for a) Random fibers b) Fibers parallel to axis of projectile c) Fibers perpendicular to axis of projectile

Table 2. Summary of Tests Performed

Run	AoO (deg)	Pitch (deg)	Yaw (deg)	Fiber Orientation
1	0	0	0	No fiber
2	0	2	2	No fiber
3	0	5	5	No fiber
4	0	0	0	Random
5	0	2	2	Random
6	0	5	5	Random
7	0	0	0	Parallel to Projectile Axis
8	0	2	2	Parallel to Projectile Axis
9	0	5	5	Parallel to Projectile Axis
10	0	0	0	Perpendicular to Projectile Axis
11	0	2	2	Perpendicular to Projectile Axis
12	0	5	5	Perpendicular to Projectile Axis

Although the model captured quite accurately the parallel, and perpendicular orientation of the projectile, it did not capture the parallel orientation (see Figure 29). The analyst and author are currently investigating the limitation observed with the preferential orientation of fibers across the width of the specimen.

Figure 30 shows the change in the z-velocity (along the axis of the projectile) of the projectile with time. The velocity is taken to be the average velocity in the Z coordinate for the projectile. For the initial velocity of 960 m/s, the velocity time curve is displayed in Figure 30a. This result illustrates an initial drop in velocity with time that coincides with the bullet loosing velocity due to the resistance of the panel. Hence, it is expected, that when the projectile velocity begins to plateau, this point represents the point of exit of the projectile of the panel. However, the results does not display exit of the bullet until about 0.16 ms. Previous numerical experiments conducted with LDPM in MARS also display this phenomenon—the bullet reduces in speed and takes a longer time to exit the specimen. Another observation from the figure is the increase in velocity when the projectile has an initial pitch of 5 degrees in the fiber reinforced specimens, which is not a typical change for a projectile exiting a target and must be further investigated. A possible explanation may be the velocity output is not accurate. Additionally, considering the velocity at which the bullet exited the panel, there was a 3% difference between the plain and the fiber-reinforced specimen. Similarly, progressing from the 0 degree pitch to 5 degree pitch caused a percent difference of approximately 2 %.

A velocity of 1500 m/s was applied to the projectile to evaluate a trend with increasing velocity. Previous perforation and penetration experiments have shown that velocities high above and below the ballistic limit of the projectile, maintain a similar response. However, for velocities close to the ballistic limit, the response of the projectile can differ considerably. A comparison of Figure 30a and b shows a similar response for the both velocities that are high above the ballistic limit of the bullet.

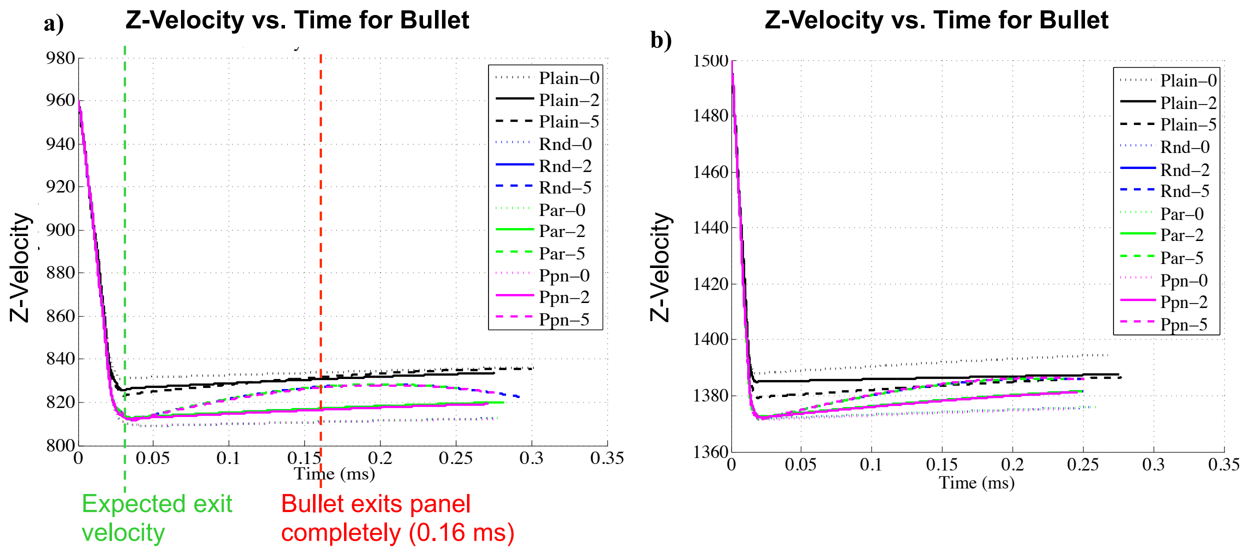

Figure 30. Change in z-velocity of projectile with time for initial speed a) 960 m/s b) 1500 m/s

In addition to the exit velocity, the orientation of the projectile on exit of the panel was determined, and the results are shown in Table 3. With the exception of the exit pitch of the plain specimen with initial pitch of 2 degrees, there is a general trend in the results. The orientation of the fibers did not generate much change in the results of the yaw and pitch upon exit of bullet. However, the change in intial pitch caused a change in the exit orientation of the projectile, and the addition of fibers to the matrix also changed the orientation. With the diameter of projectile to aggregate size ratio being about 1:4, the angles observed in the experiments can change when the aggregate size is scaled up or down.

Table 3. Results of Exit Yaw and Pitch for Projectile for Striking Velocity of 1500 m/s

Run	Fiber Orientation	Initial Pitch (deg)	Final Yaw (deg)	Final Pitch (deg)
1	No fiber	0	18	17
2	No fiber	2	31	4
3	No fiber	5	39	23
4	Random	0	17	8
5	Random	2	14	31
6	Random	5	27	69
7	Parallel to Projectile Axis	0	17	8
8	Parallel to Projectile Axis	2	14	31
9	Parallel to Projectile Axis	5	27	69
10	Perpendicular to Projectile Axis	0	17	9
11	Perpendicular to Projectile Axis	2	13	31
12	Perpendicular to Projectile Axis	5	27	67

The mesoscale crack opening in the different projectiles can be seen in Figure 31 to Figure 34. There are no visible radial cracks because the boundary conditions were all fixed on the panel edges. When fibers were added to the specimen, the crack failure was reduced. Moreover, looking at the side view of the plates shows the crack failure to occur mostly at the front half of the specimen, both in plain and fiber reinforced cases. The tunneling effect extends to the back of the panel. A possible explanation for this phenomenon is due to the projectile being modeled as rigid, which changed the crack response. A comparison of the different pitch values did not produce much change in the crack damage zone of the panels. Moreover, the back face of the panels having fibers perpendicular to the axis of the projectile, shows more crack distribution that all the other cases. Further investigation will be performed on free panels with elasto-plastic projectiles to investigate the change in crack pattern through the panel as well as the spalling effects.

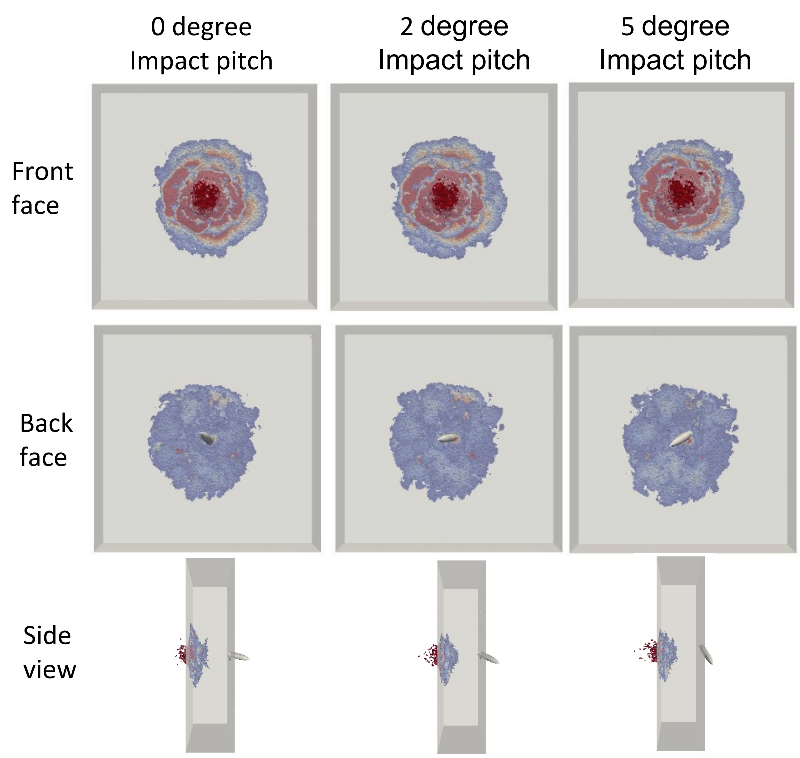

Figure 31. Crack pattern for projectile with plain panel for striking velocity of 1500 m/s

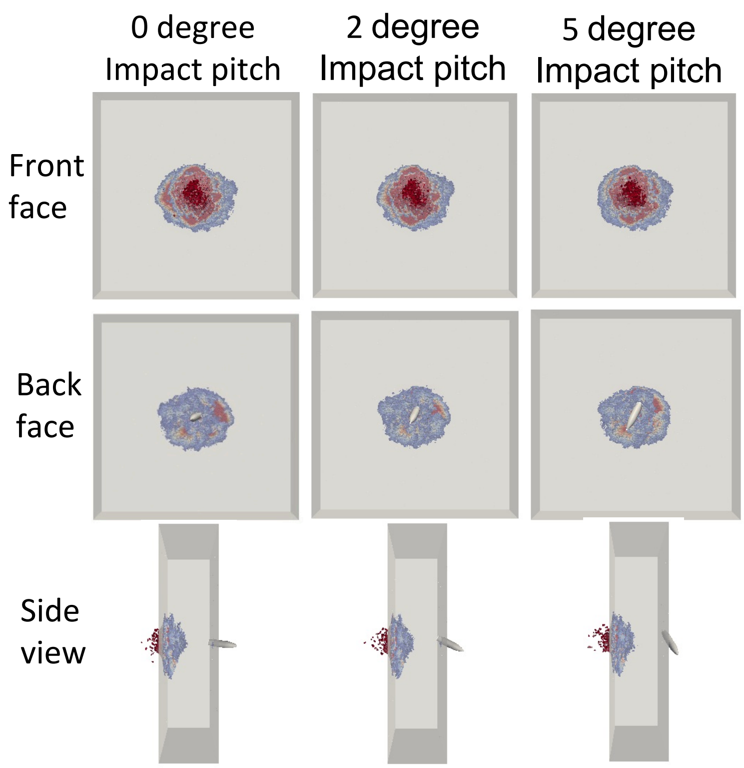

Figure 32. Crack pattern for projectile with random fiber reinforced panel for striking velocity of 1500 m/s

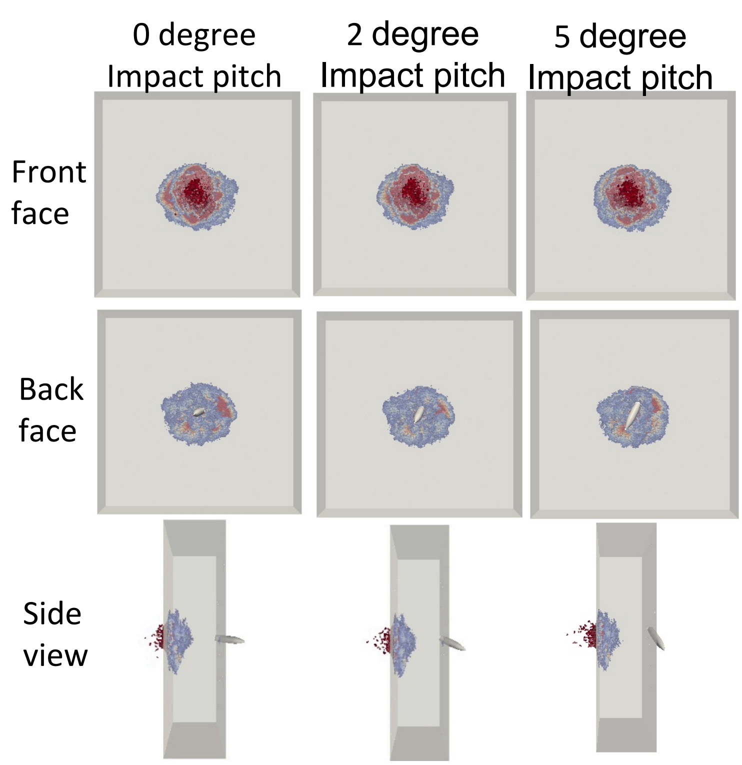

Figure 33. Crack pattern for projectile with parallel fiber reinforced panel for striking velocity of 1500 m/s

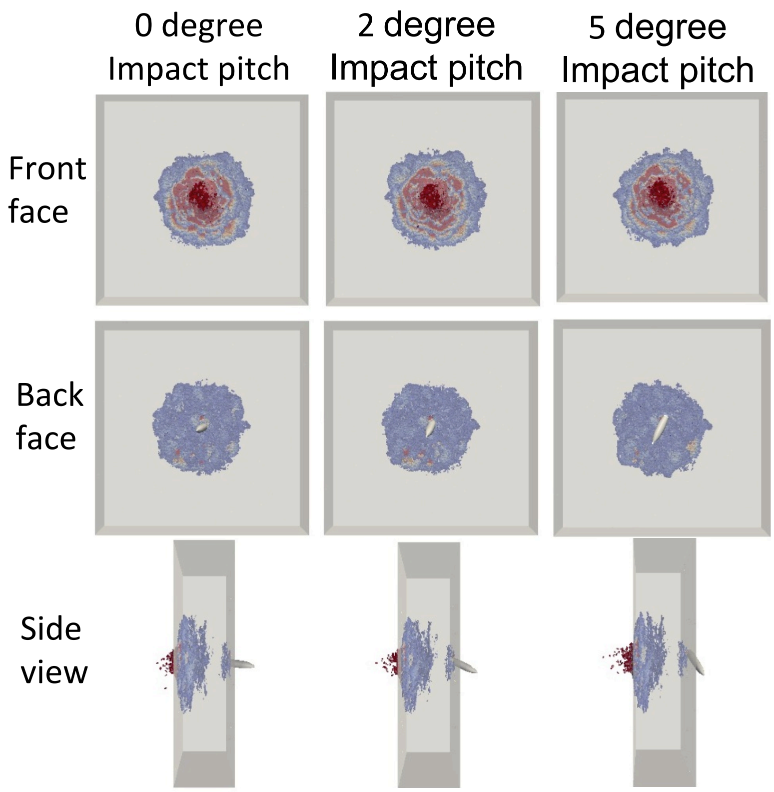

Figure 34. Crack pattern for projectile with perpendicular fiber reinforced panel for striking velocity of 1500 m/s

5. SUMMARY

The comparison of the LDPM and the K&C model for quasi-static experiments showed the importance of having a discrete model to accurately represent concrete behavior. In addition, the K&C model showed some mesh dependence, making it difficult for an analyst to achieve accurate results. In the compression regime, the K&C model was able to correctly achieve the peak load, but it severely underestimated the tensile load although the K&C model was able to capture the response in the triaxial compression from lower to higher confinement. However, the model did not capture size effect, which is essential since the K&C model is generally used to achieve a quick response of larger structural problems.

The LDPM model accurately captured the response of the model in the compression, tension, and softening regimes. Additionally, because the model is discrete it is able to show accurate crack patterns, without using additional phenomenon like element deletion. These and other LDPM results demonstrate the effectiveness of the model as a predictive tool for capturing concrete failure and fragmentation. Also, LDPM predicted the response of the perforation experiments with varying projectile speeds as well as varied fiber orientation. Consideration must be made for the coarse graining effect used in the simulations, and the effect of this assumption should be further analyzed.

The LDPM model in general is a novel and effective model that can be used to capture the response of concrete under quasi-static and dynamic loading while showing the failure patterns through its discrete framework. However, having a discrete model to represent materials with very fine aggregate sizes creates a high computation cost. Additionally, the model must first be calibrated, and the user may need some experience to perform a quick parametric identification, before the model can be applied.

BIBLIOGRAPHY

G. Cusatis, A. Mencarelli, D. Pelessone, J. Baylot. "Lattice discrete particle model (LDPM) for failure of concrete. II: Calibration and validation." *Cement and concrete composites* 33, no. 9 (October 2011): 891-905.

G. Cusatis, D. Pelessone, A. Mencarelli. "Lattice Discrete Particle Model (LDPM) for failure behavior of concrete. I: Theory." *Cement and concrete composites* 33, no. 9 (October 2011): 881-890.

G. Vasconelos, P.B. Laorenco, C.A.S. Alves, J. Pamplona. "Ultrasonic evaluation of the physical and mechanical properties of granites." *Ultrasonics* 48, no. 5 (9 2008): 453-466.

J. E. Bishop, T. E. Voth. *Semi-infinite target penetrationby ogive nose penetrators: Alegra SHISM code predictions for ideal and non ideal impacts .* Albuquerque: Sandia National Laboratories, 2009.

L. J. Malvar, D. Simons. "Concrete material modeling in explicit computations." *Workshop on recent advances in computation structural dynamics and high performance computing.* USAE Waterways Experiment Station, April 24-26, 1996.

M. S. Konsta-Gdoutos, Z. S. Metaxa, S. P. Shah. "Highly dispersed carbon nanotube reinforced cement based materials." *Cement and Concrete Research* 40, no. 7 (7 2010): 1052-1059.

R. M. Brannon, S. Leelavanichkul. *Survey of four damage models for concrete.* (SRD), SAND09-5544, Albuquerque, NM: Sandia National Laboratories,, 2009.

Smith, J. "Calibration and valication of the lattice discrete particle model for ultra high performance fiber reinforced concrete." *20th analysis and computation speciality conference.* Chicago: ASCE, 2012. 394-405.

X. Lu, C. T. Hsu. "Behavior of high strength concrete with and without steel fiber reinforcement in triaxial compression." *Cement and Concrete Research* 36, no. 9 (9 2006): 1679-1685.

DISTRIBUTION

1	MS0840	Eliot Fang	1524
1	MS0840	John Pott	1525
1	MS0845	Joe Jung	1542
1	MS1160	Aaron Brundage	5431
1	MS1160	Damon Burnett	5431
1	MS0899	Technical Library	9536 (electronic copy)

Sandia National Laboratories